CrossMark

PLASMA ENVIRONMENT AROUND COMET 67P/CHURYUMOV–GERASIMENKO AT PERIHELION: MODEL COMPARISON WITH ROSETTA DATA

H. MADANIAN[1], T. E. CRAVENS[1], J. BURCH[2], R. GOLDSTEIN[2], M. RUBIN[3], Z. NEMETH[4],
C. GOETZ[5], C. KOENDERS[5], AND K. ALTWEGG[3]
[1] Department of Physics and Astronomy, University of Kansas, Lawrence, KS, USA; cravens@ku.edu
[2] Southwest Research Institute, San Antonio, Texas, USA
[3] Physikalisches Institut, University of Bern, CH-3012 Bern, Switzerland
[4] Wigner Research Centre for Physics, Budapest, Hungary
[5] Institut für Geophysik und extraterrestrische Physik, Technische Universität Braunschweig, Mendelssohnstr. 3, D-38106 Braunschweig, Germany

ABSTRACT

The plasma environment near comet 67P/Churyumov–Gerasimenko (67P/CG) is dynamically affected by various factors, including the incident solar wind and outgassing from the nucleus. The Rosetta spacecraft MAGnetometer (MAG) instrument observations near perihelion showed crossing events into a magnetic field-free region at about 170 km from the nucleus in 2015 July at 1.26 au from the Sun. At each crossing, the magnitude of the magnetic field dropped by more than 20 nT to near zero. We compared the Ion and Electron Sensor (IES) electron differential flux energy spectrum inside and outside the crossing boundaries. The IES observations show a modest but consistent drop in electron flux for energies between 40 eV and a few hundred eV at each cavity crossing event. This drop in the electron spectra might be due to the absence or attenuation of solar wind electrons inside the observed diamagnetic regions, which might or might not be a diamagnetic cavity. There is no apparent simple linear correlation between the electron count rate measured by the IES at different energies and the magnitude of the magnetic field, however; at all energies, the highest electron count rates are recorded at the highest magnetic field magnitudes. From model-data comparisons it seems that inside diamagnetic regions, pure coma photoelectrons are not sufficient to explain the observations and that a trapping mechanism and/or infused solar wind electrons are necessary to explain the observed electron fluxes.

Key words: comets: individual (comet 67P/CG) – instrumentation: detectors – magnetic fields – plasmas – solar wind

1. INTRODUCTION

Comets have highly elliptical orbits in the solar system. The nucleus of a comet is composed of mixtures of frozen volatiles and dust, and sublimation from the surface is responsible for the loss of cometary species into the space environment (Balsiger et al. 2007; Glassmeier et al. 2007a; Gombosi 2015; Nilsson et al. 2015). Upon sublimation, the cometary neutrals expand outward and the incident solar extreme ultraviolet (EUV) photon flux photoionizes the neutral coma (Mendis et al. 1985; Cravens 1991a), creating photoelectrons and ions. High-energy electrons in the solar wind can also ionize the neutral species through electron impact ionization (Gan & Cravens 1990).

The interaction of comets with the solar wind is particularly interesting, as comets have no intrinsic magnetic field and gravity from the nucleus is negligible. A significant portion of our understanding of the cometary boundaries emerged from analyzing data from the Giotto spacecraft's encounter with comet 1P/Halley on 1986 March 14. The spacecraft entered the diamagnetic cavity at a distance of about 4500 km from the nucleus, where the magnetic field magnitude dropped by 20 nT to almost zero (Neubauer 1986, 1988) over a distance of 25 km. For comet 1P/Halley, Cravens (1986), Ip & Axford (1987), and Puhl-Quinn & Cravens (1986) showed that the force balance between the magnetic pressure gradient force from the solar wind and the ion–neutral drag force in the coma determines the stand-off distance of the field-free region boundary. This distance is known as the cavity boundary or contact surface. Flammer et al. (1991) characterized the

interaction between unmagnetized outflowing cometary plasma and inflowing magnetized solar wind plasma as a tangential discontinuity in which two scale lengths, the Larmor radius of the outflowing ions and the effective distance of the ion–neutral drag force, were determined to effectively describe the structure of the discontinuity. During the interaction, the cometary ions will be subjected to the Lorentz force from the frozen-in Interplanetary magnetic field and the motional electric field of the solar wind, and will be assimilated into and picked up by the solar wind (Neubauer 1988; Cravens 1989). Momentum conservation will cause the mass-loaded solar wind, which initially moves at supersonic speeds, to slow down to subsonic speeds and deflect (Broiles et al. 2015; Behar et al. 2016). The transition of the solar wind from supersonic to subsonic speeds produces a bow shock upstream of the comet (Omidi & Winske 1987; Coates et al. 1991, 1997; Coates 2009). Consequently, the solar wind magnetic field lines drape around the comet and pile up in its sunward side (Eviatar & Goldstein 1988; Cravens & Gombosi 2004). Within the stand-off distance, inside the diamagnetic cavity, the ions and neutrals move radially outward and interact with the magnetic field pile-up region (Ip & Axford 1987). Neutral species are not affected by the enhanced magnetic field while cometary ions are likely to pile up as they approach the region of enhanced magnetic field. Electron–ion recombination has been shown to be a major sink for ions in the region just outside of the cavity surface (Goldstein et al. 1989; Cravens et al. 1995; Puhl-Quinn & Cravens 1995).

For comet 67P/CG, some of these boundaries and regions may only be observed near perihelion when the comet is more

active and collisional processes in the neutral coma become more frequent. The characteristics of these boundaries can also be quite different from comet 1P/Halley. For comet 67P/CG, at 3 au and at close proximity to the nucleus, the measured flux of suprathermal electrons was much higher than the regular solar wind (Madanian et al. 2016a). The photoionization of a weak coma, compression, and ambipolar electric field were the likely contributing sources to the electron population. It was also shown that, within 100 km from the nucleus, the collisional cooling of suprathermal electrons is significant and helps to build up high thermal electron densities. The cometary electrons can also be characterized with kappa distributions, a combination of two dense and warm (thermal) and rarefied and hot (suprathermal) populations (Broiles et al. 2016). By comparing the cometary electron environments for an inactive comet at 3 au and an active comet near perihelion, Broiles et al. (2016) found that the density of hot electrons increased by a factor of 10 while the density of thermal electrons increased only by a factor of 3. The kappa indices remained the same while the thermal electrons temperature cooled by a factor of 2. So it was suggested that the hot suprathermal electrons are most likely of solar wind origin. Extreme solar events such as coronal mass ejections compress the cometary plasma upon impact and cause enhancements in the suprathermal electron densities, as well as the background magnetic field (Edberg et al. 2016).

In this paper we will follow up on the work of Goetz et al. (2016), Mandt et al. (2016), and Nemeth et al. (2016) to study and compare the plasma environment inside and outside diamagnetic regions that were observed by the *Rosetta* spacecraft at comet 67P/CG. The interpretation adopted by the above papers is that these regions were associated with the spacecraft going into and out of a diamagnetic cavity. We will largely adopt this interpretation in the current paper, recognizing that it is not the only possible interpretation (Huang et al. 2016). The goal of this paper is to interpret the data from the Ion and Electron Sensor (IES) (Burch et al. 2007) and MAGnetometer (MAG) (Glassmeier et al. 2007b) instruments, which are part of the *Rosetta* Plasma Consortium (RPC) (Carr et al. 2007) on board the *Rosetta* spacecraft. We will show the IES suprathermal electron differential flux drops at different energies during the diamagnetic cavity crossing events, and how the electron counts change depending on the magnitude of the magnetic field. We also model electron differential fluxes inside and outside a diamagnetic cavity.

The paper is organized as follows. A brief overview of the instruments is provided in Section 2, the electron and magnetic field observations for selected time periods are shown in Section 3, the results of our models are discussed in Section 4, Section 5 includes interpretation and discussion of the cavity boundary, and conclusion points are provided in Section 6.

2. INSTRUMENT OVERVIEW

The *Rosetta* spacecraft was launched in 2004 and reached comet 67P/CG in 2014 August at a heliocentric distance of 3.6 au. The spacecraft has been escorting the comet since then and through perihelion in 2015 August, at 1.24 au heliocentric distance. Multiple instruments on board the spacecraft have been measuring the changes in plasma environment during this time. These measurements are expected to continue until the end of the mission in 2016 September when the spacecraft reaches a heliocentric distance of about 3.8 au.

The IES is a set of two toroidal top-hat electrostatic analyzers that measure ions and electrons with energies between 4.3 and 17,843 eV (Burch et al. 2007). The emphasis of this paper is on the electron sensor of the IES. The energy resolution of the energy bins depends on the instrument operation mode, and for the data presented in this paper the energy resolution is 8%. The sensor has a $360° \times 90°$ field of view which is divided between 16 azimuthal panels and 16 polar elevation steps, giving a resolution of $22°.5 \times 6°$ for the observations. Due to data transfer constraints, the instrument operational mode is set up in such a way that counts from every pair of adjacent azimuth panels and elevation steps are averaged before data downlink. Unfortunately, after many months of operation, half of the azimuthal panels were not able to record low-energy electron counts properly (more discussion on this in Broiles et al. 2016). However, those unhealthy panels do not include the sunward direction panels which detect most of the nominal electron flux from the Sun direction. Whether these faulty panels affect the efficiency of other panels or the efficiency of the whole instrument is unclear.

Figure 1 shows sample data from the IES and MAG instruments between 2015 July 25 and August 1. The IES electron count rates are shown in the top panel. The counts have been summed over all elevation and azimuth angles of the IES field of view. The shaded areas between the dashed lines on July 26 and 29 mark selected time periods with a number of cavity crossing events which will be analyzed in more detail in the next section.

The electron differential fluxes in this paper are calculated in a similar way as described by Madanian et al. (2016a). Note that the electron differential flux for a given direction and energy can be calculated from:

$$\frac{d\varphi}{dEd\Omega} = \frac{C'_{\text{panel}}}{G_{\text{panel}} \times E} \tag{1}$$

where $\frac{d\varphi}{dEd\Omega}$ is the differential flux of electrons, C' is the count rate of electrons measured by the instrument, E is the energy of the counted electrons, and G is the instrument geometric factor. The current available geometric factor in Burch et al. (2007) is the same for all the detection panels of the IES; however, other studies have used a set of direction-dependent and energy-dependent geometric factors for the IES sensor (Broiles et al. 2016). The IES electron differential fluxes are averaged for a set of preferred detection panels which avoid blocked viewing angles and faulty sectors (Madanian et al. 2016a).

Information on the magnetic field is obtained by the MAG instrument which is composed of two 3-axis fluxgate magnetometers (one inboard and one outboard) both mounted on a 1.5 m boom with 15 cm separation in between (Glassmeier et al. 2007b). Since the two magnetometers are closely positioned to the spacecraft, the magnetic field measurements are most likely contaminated by noise from its other instruments and components. Comparison of the registered signals by the inboard and outboard sensors shows that the spacecraft noise is affecting the inboard sensor three times more than the outboard (Richter et al. 2011). Entering the magnetic field-free regions allowed the MAG instrument team to calibrate the sensors and produce more reliable data. The bottom panel of Figure 1 shows the three components of the magnetic field in the cometocentric solar equatorial (CSEQ) system where the $+x$ direction is toward the Sun, the $+z$
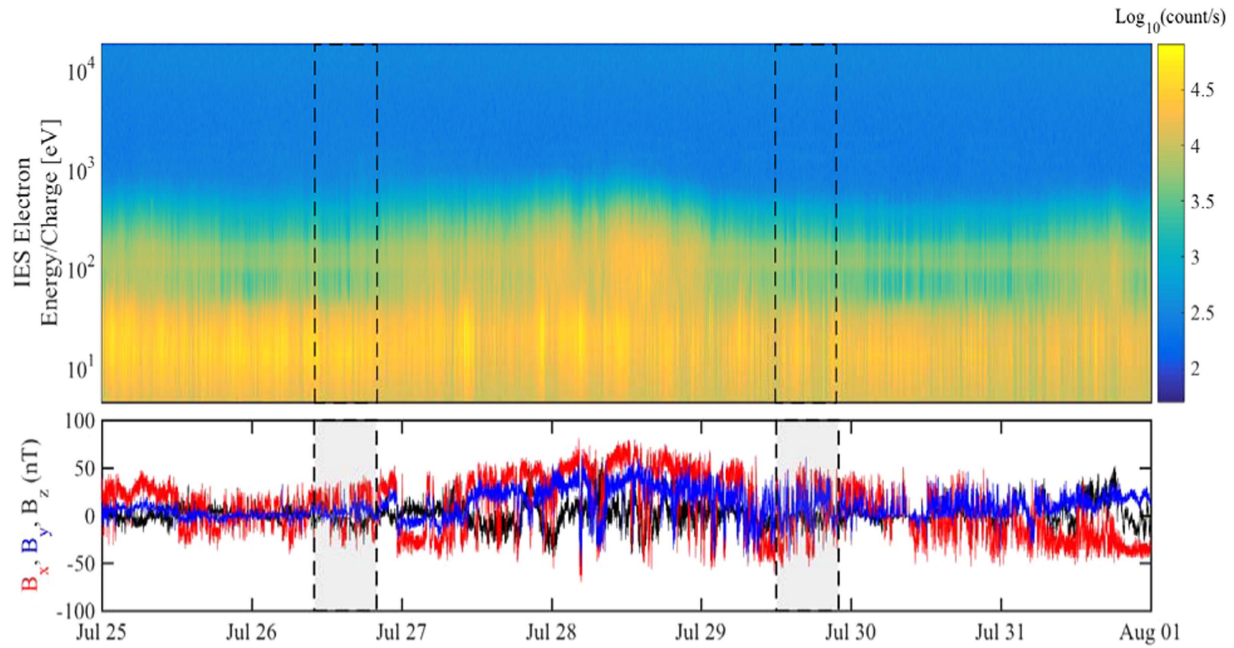
Figure 1. (Top) IES measured electron count rate from 2015 July 25 to August 1. The count rates are for the full field of view of the IES. (Bottom) Three components of the magnetic field measured by MAG in cometocentric solar equatorial coordinates for the same time period. The shaded regions between the dashed lines are the selected time periods when cavity crossing events have been observed. These data will be analyzed in more detail in the text.

direction is perpendicular to the ecliptic plane, and the $+y$ completes the right-hand rule. In Figure 1, the magnetic field measurement cadence is one second, averaged over one minute, while the IES cycle time is 256 s.

3. OBSERVATION OF THE DIAMAGNETIC CAVITY OF COMET 67P/CG

Comet 67P/CG is significantly less active than comet 1P/ Halley (between a few hundred to a few thousand times, depending on the heliocentric distance) and the meager coma of this comet may not allow for the formation of typical stable cometary boundaries. However, a magnetic pile-up region at comet 67P/CG was observed even before perihelion, at 1.5 au, caused by a sudden increase in solar wind dynamic pressure (Volwerk et al. 2016). For an extended time period around perihelion, Mandt et al. (2016) characterized a collisionopause boundary at comet 67P/CG. The location of this boundary is also affected by the nucleus outgassing rate and the solar wind dynamic pressure. This boundary, that was assumed to be outside of the diamagnetic cavity, was characterized by enhanced magnetic field pile-up, reduced electron densities, and accelerated water-group ions on the outside, and reduced magnetic field pile-up, enhanced electron densities, and low-energy water-group ions on the inside (Mandt et al. 2016).

Following extended calibration efforts on the MAG data, Goetz et al. (2016) showed the first detection of the diamagnetic cavity at comet 67P/CG near perihelion. In 2015 July and August, MAG data showed instances of the *Rosetta* spacecraft crossing a barrier within which the magnetic field magnitude plummeted from about 30 nT to near zero (Goetz et al. 2016). Two of these events are marked in Figure 1. For the event on July 26, the MAG data showed that the spacecraft spent about 25 minutes inside a diamagnetic cavity. This event is one of the longest times that the spacecraft spent inside the diamagnetic cavity. The longest event occurred on 2015 November 20, lasting 40 minutes.

Time series of IES measured electron fluxes during the observed diamagnetic cavity event on July 26, between 10:00:00 to 20:00:00 UTC, are shown in the top panel of Figure 2. The IES fluxes of 21, 47, 99, and 202 eV electrons are shown with red, green, blue, and gray lines, respectively. The bottom panel of Figure 2 shows the magnetic field magnitude for the same time period. The very low, disturbance-free region between the dashed–dotted lines, between 15:20:00 and 15:50:00 UTC, is identified as a magnetic field-free region (i.e., diamagnetic cavity). The data show a decrease of high-energy electron fluxes by about a factor of 2. It should be noted that there are other short instances of near-zero field strength, such as around 13:20:00 UTC, which are not discussed. The vertical solid lines on this panel mark the individual timestamps used to compare the full electron energy spectra inside and outside the cavity.

Figure 3 shows the full IES electron energy spectra for these timestamps. The red and yellow curves are electron energy spectra inside the cavity; the blue curve is for outside, before entering the cavity, and the purple curve is for outside, after leaving the cavity. This figure shows a wider energy range for the reduction of electron fluxes. The flux of electrons with energies between 40 eV to a couple of hundred eV has decreased when the spacecraft is in the cavity. This drop is more noticeable for 60–100 eV and 150–200 eV electrons (Nemeth et al. 2016). This signature in IES electron data was used by Nemeth et al. (2016) as a search criterion to identify the cavity crossing events. A cross-comparison of the MAG cavity observations with the cavity crossing events identified by the IES electron signature is in progress.

The event on July 26 is a prolonged period where the spacecraft extensively probed the diamagnetic cavity plasma. The other shorter incidents of magnetic field drop out, such as events on July 29, also could be considered as occurring in a magnetic field-free region. We will show that the events on
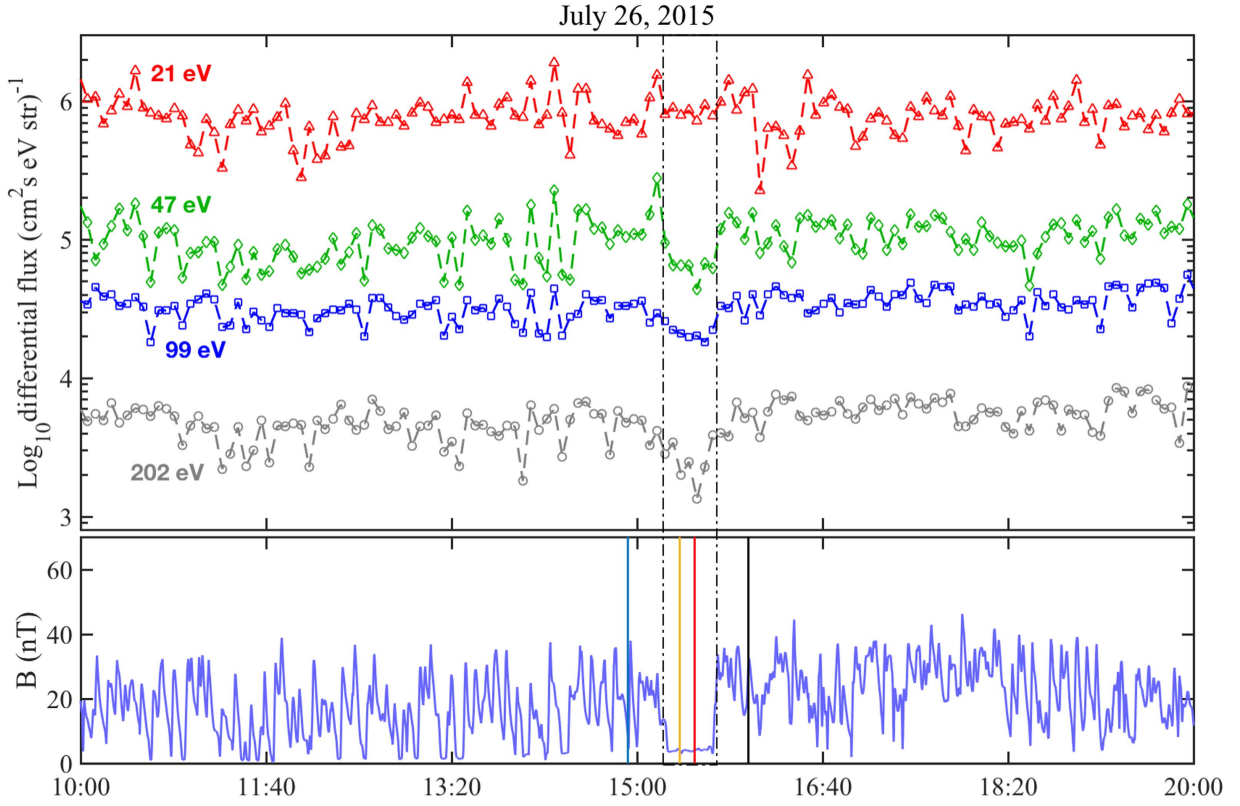
Figure 2. IES and MAG data between 10:00:00 and 20:00:00 UTC on 2015 July 26. The top panel shows the time series of IES electron fluxes for four different energy channels, 21 eV (red), 47 eV (green), 99 eV (blue), and 202 eV (gray). The bottom panel shows the magnitude of the magnetic field measured by MAG for the same time period. The two dashed-dotted lines show the time when the spacecraft was inside the cavity. Four other solid vertical lines mark the timestamps for which complete energy spectra are shown in Figure 3. Two timestamps are inside the cavity (yellow and red), one before entering the cavity (blue), and one after exiting (black).
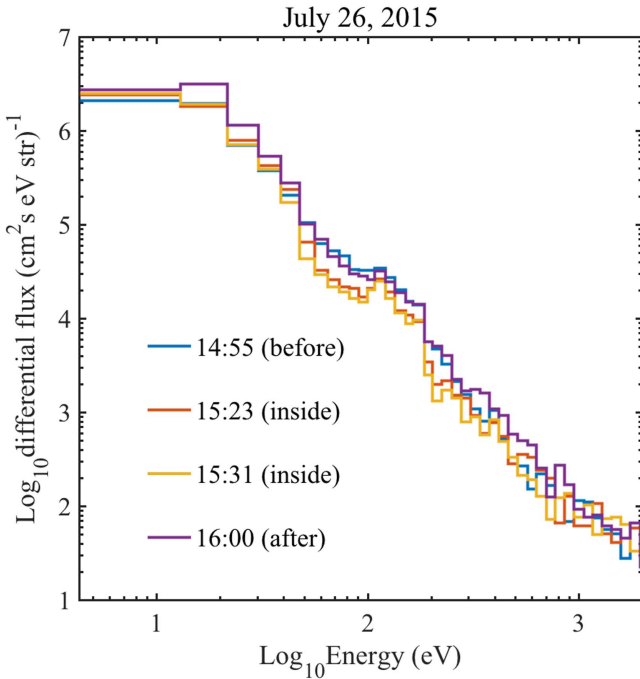

Figure 3. Energy spectrum of the IES electron differential flux for four individual timestamps on 2015 July 26. The blue spectrum is from 14:55:00 UTC where *Rosetta* has not yet crossed the cavity boundary. The red and yellow spectra are from 15:23:00 and 15:31:00 UTC when *Rosetta* is considered to be inside the diamagnetic cavity. The spectrum from 16:00:00 UTC (the purple line) shows the measured electron spectrum after the spacecraft left the cavity.

July 29, however short, still show common plasma characteristics.

The IES and MAG plasma measurements of cavity crossing events on July 29, between 12:00:00 and 22:00:00 UTC, are shown in Figure 4. The top panel shows the time series of the IES electron flux and the bottom panel shows the magnetic field strength, and the cavity crossing events are marked with dashed rectangles. The electron fluxes at some specific energies show a considerable drop each time the magnitude of the magnetic field approaches zero (i.e., spacecraft crosses the cavity boundary).

The full electron energy spectra for selected timestamps on July 29 are shown in Figure 5. There are similarities between the electron spectra inside the cavity in this figure and those shown in Figure 3 for July 26. The flux of electrons with energy between 40 eV to a few hundred eV tends to decrease inside the magnetic field drop-out regions. More noticeable declines are seen for electron energies between 60–90 eV and 150–200 eV.

The IES observations show a modest but consistent drop in electron flux for energies between 40 eV and a few hundred eV at each cavity crossing event. In general, the difference in electron flux inside and outside of the cavity is not dramatic. A difference of about a factor of 2 is seen for energies between 40 eV and a couple of hundred eV. There are larger differences at some specific energy ranges, such as 60–90 eV and 200–250 eV. The fluxes with energies less than ∼40 eV either do not change, such as on July 26, or show a small increase, as for the July 29 event.
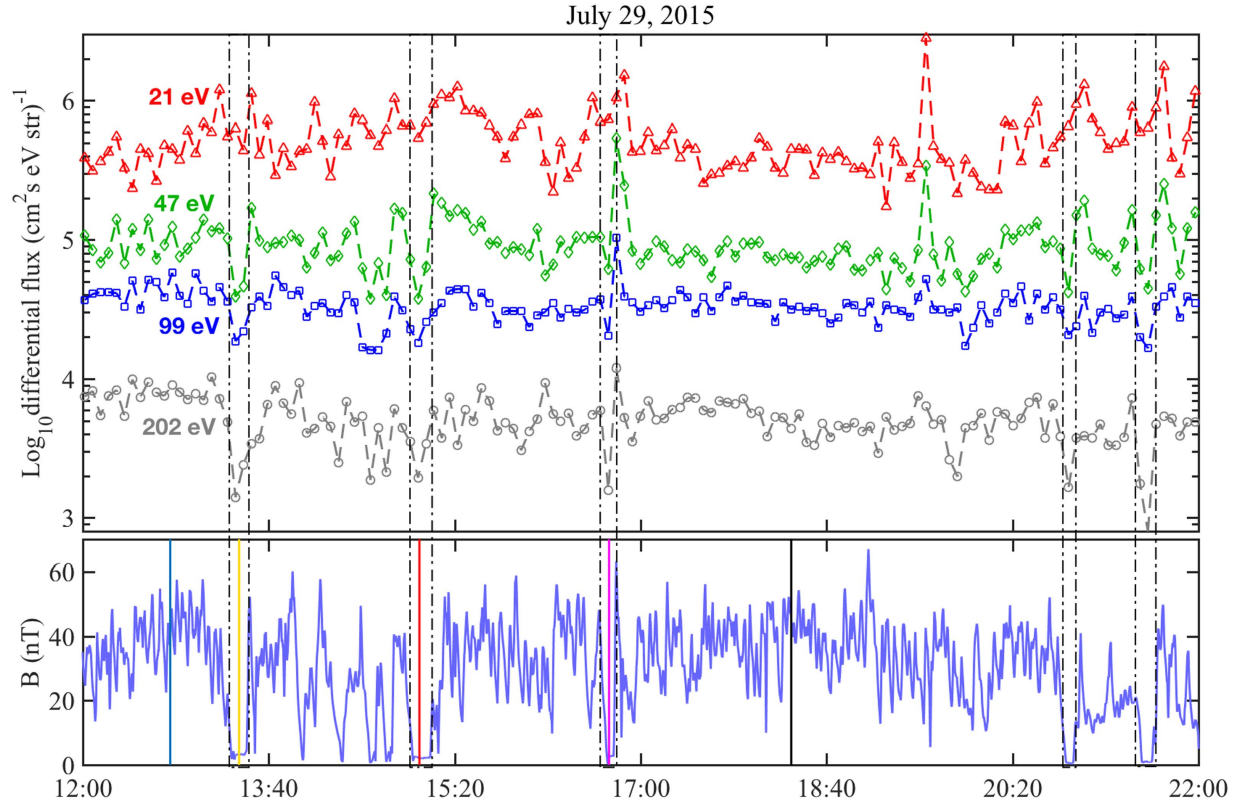
July 29, 2015

Figure 4. Similar to Figure 2 but for the events on 2015 July 29 between 12:00:00 and 22:00:00 UTC. The top panel shows the time series of the IES electron differential flux with energies 21 eV (red), 47 eV (green), 99 eV (blue), and 202 eV (gray). The bottom panel shows the magnitude of the magnetic field measured by MAG for the same time period. The dashed rectangles on this panel mark the cavity crossing events. The solid lines are drawn at selected timestamps for which the energy spectrum is shown in Figure 5. The blue and black lines are for spectra outside of the cavity and yellow, red, and purple lines correspond to spectra inside the cavity.
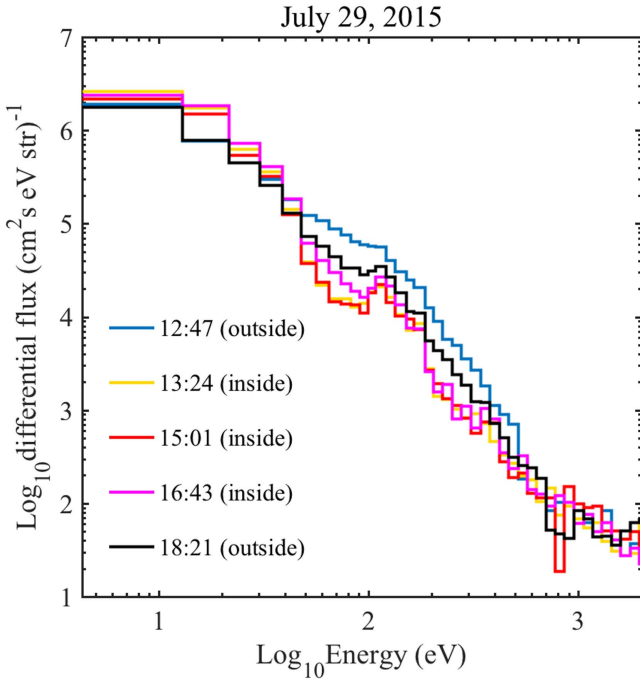
July 29, 2015

Figure 5. Electron differential flux energy spectra for five individual timestamps on July 29. The blue and black lines show the measured spectra outside the cavity and yellow, red, and purple lines correspond to observed spectra inside the cavity.

It is important to realize that these observations were made while the spacecraft was escorting the comet and was hovering in the flank region, unlike comet 1P/Halley's observations which were made during a transiting flyby. So it is unlikely that the spacecraft is moving through the plasma boundaries, but rather the plasma boundaries are expanding and contracting.

We also looked at the correlation between the measured electron counts and the magnitude of the magnetic field for data from 2015 July 1 to August 31. This is the time period when the comet is highly active and the cavity boundary is most likely to be present. The count rates of electrons at four different energies versus the magnitude of the magnetic field are shown on the scatter plots of Figure 6. The IES electron counts are summed over all elevations and azimuth angles. Due to the difference in measurement cycles, IES and MAG measurement timestamps had to be matched first. The data points are colored based on the observation time, as shown by the color bar on the right. The four panels in Figure 6 show scatter plots of 13, 99, 151, and 203 eV electrons versus magnetic field strength. The dashed rectangle at the bottom of each plot distinguishes near-zero magnetic field strength (below 15 nT) observations, or the counts inside the diamagnetic cavity. Due to uncertainties in the MAG measurement and calibration, a range of weak field strengths is selected to represent the observations inside and around the cavity boundary rather than an absolute zero field.
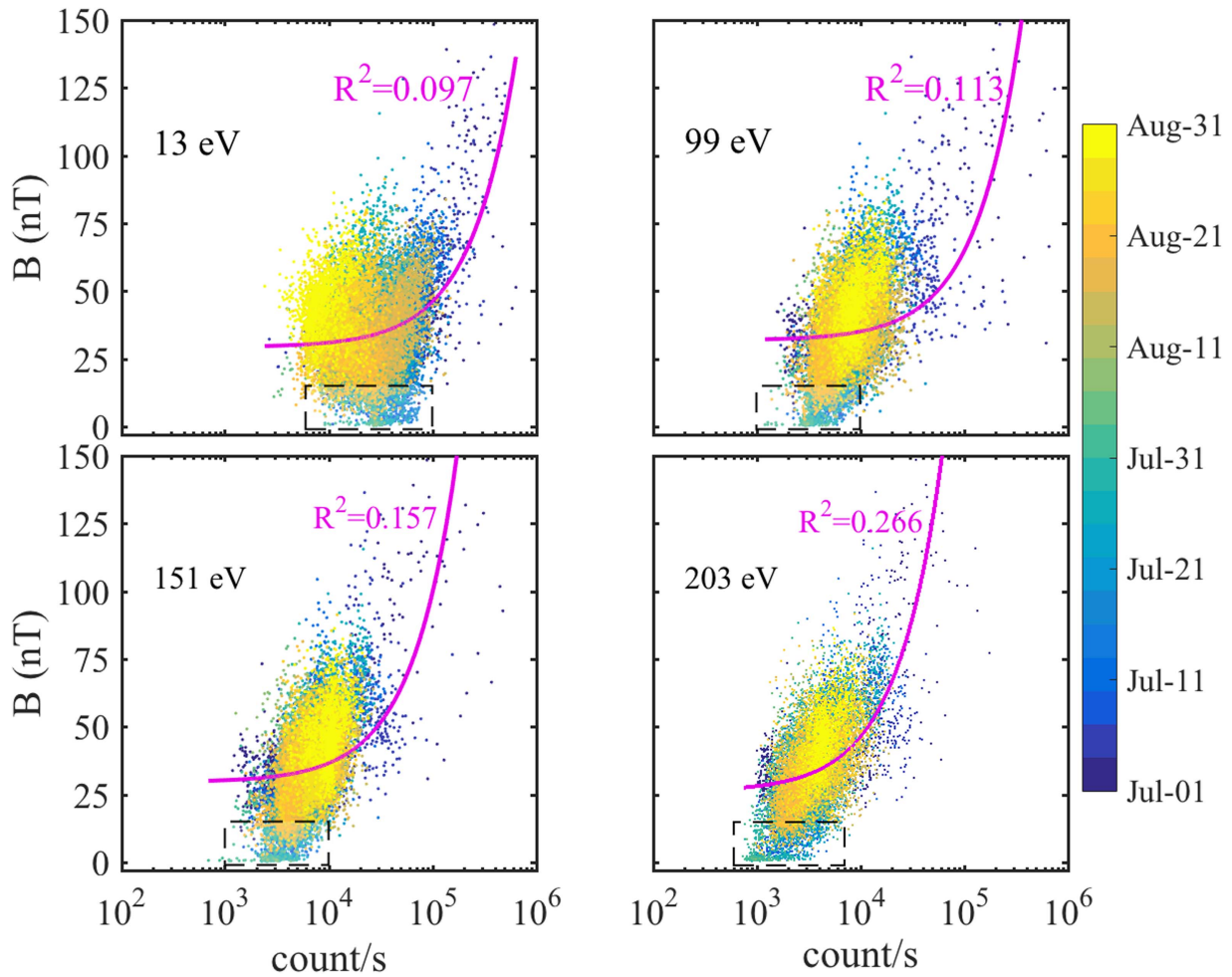
Figure 6. Electron count rates measured by the *Rosetta* RPC-IES sensor vs. the magnitude of the magnetic field measured by the MAG instrument for electron energies of 13, 99, 151, and 203 eV. The data points are color coded based on the date of the observations from 2015 July 1 to August 31. The color bar shows the corresponding time. The purple line on each plot shows the linear fit on the data with R^2 goodness-of-fit shown next to each curve. Dashed rectangles at the bottom of each plot mark the observations inside the diamagnetic cavity which correspond to the lowest values of the magnetic field magnitude.

The count rates in each panel of Figure 6 were linearly fitted (the purple curves) to check for linear correlation between the magnitude of the magnetic field and electron counts. The R^2 goodness-of-fit is shown on each panel. No apparent linear correlation can be seen in the fitted curves. A more sophisticated statistical analysis of the data should be undertaken.

At high magnetic field strengths more electron count variations are observed, and fewer variations when the spacecraft is in the cavity. For instance, for the 13 eV electrons, count rates of about 3×10^4 s^{-1} are observed when the magnetic field magnitude is close to the minimum. On the other hand, in channel 151 eV, the count rate is about 2000–3000 s^{-1} for lowest values of the magnetic field. Inside the cavity, the count rates have a narrow range while outside the cavity the electron count rates have a wider range of values. Also, for low-energy electrons the count rate inside the cavity is not necessarily a minimum, but for high-energy electrons the minimum count rates occur at the lowest strengths of the magnetic field, or when the *Rosetta* spacecraft is inside the diamagnetic cavity.

4. MODELING THE ELECTRON FLUX NEAR THE POSSIBLE CAVITY BOUNDARY OF COMET 67P/CG

Several modeling attempts have been performed to estimate the position of the diamagnetic cavity and other cometary boundaries around comet 67P/CG (Koenders et al. 2013, 2015; Rubin et al. 2014). The hybrid model of Koenders et al. (2015), where ions are treated as kinetic particles and electrons as a massless fluid, showed that the diamagnetic cavity barrier is positioned at distances less than 50 km from the comet in the Sun–comet direction. It should be noted that the total gas production rates assumed pre-encounter seem to be much lower than the measured values by the *Rosetta* Orbiter Spectrometer for Ion and Neutral Analysis (ROSINA) Cometary Pressure Sensor (COPS) (Hansen et al. 2016). Also, the reported distances can increase by a factor of one and a half near the terminator plane regions. The stand-off position of the bow shock was also predicted to be at around 2000 km from the comet, which is much less than the solar wind ion gyroradius (Koenders et al. 2013). This is perhaps why the boundaries and plasma regions of comet 67P/CG do not resemble the cometary plasma of other previously visited comets.

Magnetohydrodynamic (MHD) models (electrons and ions are treated as fluids) have shortcomings in modeling the structure of the plasma around the comet (Hansen et al. 2007). However, the improved multifluid MHD model of Rubin et al. (2014) showed that draping of the magnetic field lines and gyration of the ions near the comet are in agreement with hybrid model results. These models predicted that the cause of instabilities in the magnetic field, such as those seen in MAG data (Goetz et al. 2016), can be due to asymmetric outgassing from the nucleus or a sudden drop in the solar wind dynamic pressure (Rubin et al. 2012; Koenders et al. 2015; Richter et al. 2015).

Suprathermal electrons are produced in two ways in our model (see Madanian et al. 2016a): (1) production of photoelectrons from photoionization of the neutral coma, and (2) injection of solar wind electrons from outside the inner coma. Suprathermal electrons with high enough energy can create secondary electrons through electron impact ionization. H^- ions (Burch et al. 2015) and negatively charged nanograins are also sometimes seen by the IES at certain energies, due to double charge exchange between the solar wind protons and the water molecules. But those processes are not included in our model. The incident solar photon flux in the EUV and soft X-ray range is modeled using the EUVAC and SOLAR2000 solar irradiance models (Madanian et al. 2016a). The photo-absorption and the photoionization cross sections for water, CO_2, and CO are used to calculate the electron production rate in the coma as a function of radial distance from the nucleus (Gan & Cravens 1990; Cravens 1991b). The photoelectrons were tracked using a two-stream methodology (Nagy & Bank 1970) in which it is assumed that inside the cavity the electron motion, on average, is either toward the comet or away from it. The magnetic field line geometry for outside of the cavity is a parabola shape to resemble the draped magnetic field around the comet (Madanian et al. 2016b). The electron impact ionization cross sections of water, CO_2, and CO were used to calculate the secondary electron production rates (Cravens et al. 1987). Note that we neglected any surface photoelectrons that might be produced. Figure 7 shows modeled differential fluxes of electrons for different circumstances, as well as two IES-measured electron flux spectra from inside the diamagnetic cavity.

For the first model case, we simulated the electron differential flux from pure photoionization of the neutral coma with no solar wind electrons (gray curve in Figure 7). Note that the energy resolution of the model results is much higher than the IES energy resolution. However, the model results have been sorted into an energy bin structure similar to the IES instrument for easier comparison. The visible peaks in the spectra around 30 and 100 eV correspond to the features in the solar irradiance spectrum. The nucleus outgassing rate for all model runs was selected at $Q = 5 \times 10^{27}$ s^{-1} and the distance to the comet nucleus is around 150 km at a heliocentric distance of 1.25 au. More details of the model parameters are provided in Table 1. These values are comparable to the *Rosetta* measurements and position during the cavity crossing events in late July.

For the second model case, solar wind electrons were injected as a boundary condition in the model in the form of a flux of electrons with bi-Maxwellian distribution. In Figure 7, two separate cases with solar wind electrons are shown. The red curve is for a weak (low-density) solar wind which
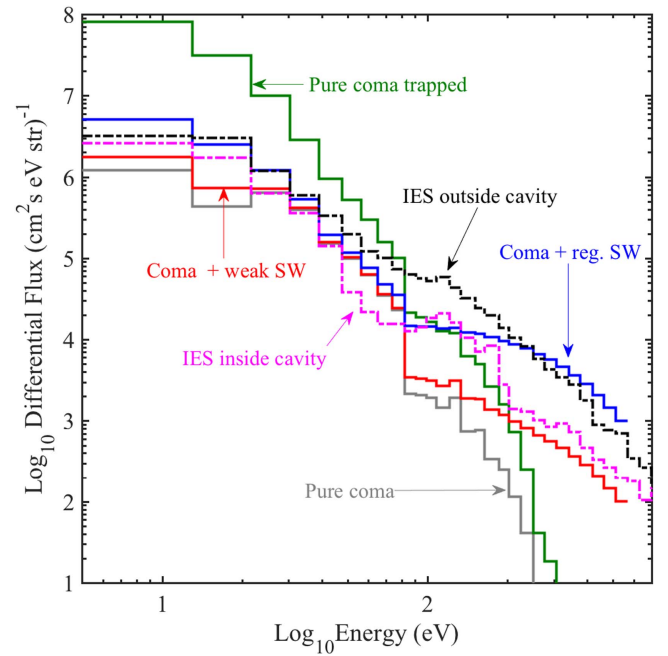

Figure 7. Model spectra for differential flux of electrons for pure coma photoelectrons (gray), coma photoelectrons with attenuated (weak) solar wind boundary condition (red), coma photoelectrons with regular solar wind condition (blue), and trapped pure coma photoelectrons with reflecting boundary condition (green). Two IES electron spectra from 2015 July 26, one for inside the diamagnetic cavity (the dashed magenta curve) and one for completely outside the cavity (the dashed black curve) are shown for comparison. The nucleus gas production rate for all model cases was chosen to be at 5×10^{27} s^{-1} and the distance to the comet is at 150 km and the heliocentric distance of 1.25 au, comparable to the *Rosetta* measurements and position. More details of the model parameters are given in Table 1.

Table 1
Model Parameters

Photoionization	
Solar flux irradiance $F_{10.7}$:	118 sfu
Heliocentric distance:	1.25 au
Model subsolar point:	150 km
Nucleus outgassing rate:	5×10^{27} s^{-1}
Neutral density profile:	$n(r) = \frac{Q}{4\pi r^2 u_n}$
Outflow velocity:	$u_n = 1$ km s^{-1}

Solar wind boundary flux parameters (at 1 au) Regular solar wind:	
n_{core}:	7.0 cm^{-3}
T_{core}:	5 eV ($\sim$6 $\times$ 10^4 K)
n_{halo}:	0.2 cm^{-3}
T_{halo}:	100 eV ($\sim$10^6 K)

Weak (attenuated) solar wind:	
n_{core}:	1.0 cm^{-3}
T_{core}:	5 eV ($\sim$6 $\times$ 10^4 K)
n_{halo}:	0.01 cm^{-3}
T_{halo}:	100 eV ($\sim$10^6 K)

represents an attenuated solar wind flux that would be observable inside the cometary bow shock but still outside the diamagnetic cavity. The blue curve is for a regular solar wind electron density which would correspond to the electron

environment completely outside the diamagnetic cavity. The densities and temperatures of the solar wind core and halo populations that are used at the model boundary are given in Table 1.

To simulate the buildup of electrons inside the diamagnetic cavity, for the next model case we constrained the motion of electrons by trapping all the coma photoelectrons in the region by a reflecting boundary condition, so that the photoelectrons will remain within about 150 km from the nucleus and interact with the neutral coma. No solar wind electrons are introduced at the boundary for this case. The result of this case is shown with the green curve on Figure 7. Two IES electron spectra from July 26, one for inside the cavity (the dashed magenta curve) and one for entirely outside the cavity (the dashed black curve), are also over-plotted for comparison.

5. INTERPRETATION AND LOCATION OF THE CAVITY BOUNDARY

It has been shown that at comet 1P/Halley, the thermal pressure of the cometary plasma is not sufficient to balance the solar wind pressure (i.e., not a Venus-like ionospheric balance). Instead, force balance between the ion–neutral drag force and the magnetic pressure determines the position of the cavity boundary (Cravens 1986, 1989; Ip & Axford 1987). The simple one-dimensional (along the radius) model of Cravens (1986) reasonably simulated the structure of the magnetic field near the cavity boundary at comet 1P/Halley, where it was assumed that a magnetic field pile-up region exists upstream of the diamagnetic cavity. A similar concept can be applied to comet 67P/CG to approximately estimate the position of the cavity boundary (Goetz et al. 2016). We estimated the diamagnetic cavity distance around comet 67P/CG using a similar approach.

The water group ions, specifically H_3O^+, are the most abundant ion species in the coma of an active comet (Vigren & Galand 2013; Nilsson et al. 2015). The H_3O^+ is produced through the fast reaction of H_2O^+ with water molecules (Korosmezey et al. 1987):

$$H_2O^+ + H_2O \rightarrow H_3O^+ + OH \quad k_{in} \approx 1.1 \times 10^{-9} \, cm^3 \, s \quad (2)$$

where k_{in} is the ion–neutral collision rate. H_3O^+ is consumed by electron dissociative recombination (Goldstein et al. 1989; Flammer et al. 1991; Damas & Mendis 1992; Flammer 1993; Cravens et al. 1995). The structure of the magnetic field as a function of distance and outgassing rate can be calculated from (Cravens 1986, Equation (19); Cravens 1989):

$$B(r) = B_0 \sqrt{1 - \left(\frac{r_{cs}}{r}\right)^2} \quad (3)$$

where r is the distance to the comet, r_{cs} is the boundary or stand-off distance, and B_0 is the maximum magnitude of the stagnant magnetic field upstream of the comet. B_0 is an independent parameter and can be considered as a proxy for solar wind dynamic pressure (Cravens 1989). The stand-off distance of the cavity boundary is highly sensitive to the outgassing rate from the nucleus and the maximum stagnant magnetic field. At a distance of $r = r_{cs}$, the magnitude of the

magnetic field is zero and r_{cs} can be found from:

$$r_{cs} = 7.08 \times 10^{-18} \frac{Q^{\frac{3}{4}}}{B_0} [cm]. \quad (4)$$

In this equation, B_0 is in Gauss, and Q is the nucleus outgassing rate in s^{-1}.

We used Equation (4) to calculate the position of the cavity boundary based on *Rosetta* measurements of outgassing rate and magnetic field from 2015 July 20 to August 10. The neutral outgassing rates are from ROSINA/COPS (Balsiger et al. 2007). The B_0 values were found by searching for local maxima (peaks) in the magnetic field data according to the following criteria: (1) peak values must be greater than 30 nT, (2) the minimum prominence is 20 nT, and (3) the minimum time between two adjacent peaks is one minute. The corresponding (or closest available) outgassing rates and magnetic field magnitudes at the peak points are then used in Equation (4) to estimate the position of the cavity.

The results of this simple approach are shown in Figure 8. The top panel shows the magnetic field magnitude in nT in black. The local peak points are shown with yellow circles. The middle panel is the nucleus outgassing rate. The sinusoidal changes on this curve correspond to the 12 hour rotational period of the comet and the northern lobe having a higher outgassing rate than the southern lobe. The bottom panel shows the *Rosetta* spacecraft trajectory (blue line) and the modeled cavity boundary distances (r_{cs}). The two red vertical dashed lines show two cavity crossing events on 2015 July 26 and 29.

The estimated r_{cs} agree reasonably well with the observed distances of the two cavity crossing events on July 26 and 29 (Goetz et al. 2016; Nemeth et al. 2016; and Mandt et al. 2016) which were at about 170 km from the nucleus. The estimated boundaries in Figure 8 show that the spacecraft should have been inside the diamagnetic cavity on July 30 or August 3. And in fact, a closer look at the MAG data for these dates shows that the magnetic field strength on July 30, in a few instances, dropped to the lowest values. But on August 3 the magnetic field did not show a reduction, where our model predicted the *Rosetta* should be in the cavity. So discrepancies can be due to the fact that this model only provides a rough estimate of the cavity boundary and many plasma complexities were not taken into account. Also, outgassing rates and magnetic field measurements can be highly error prone. For instance, the outgassing rate is only an approximation of the total production rate and is deduced from a single point measurement at the location of *Rosetta*.

Note that the estimates of the diamagnetic cavity boundary in Figure 8 are based on a Halley-type cavity, which might not be entirely correct. Even though the model predicted stand-off boundary distances reasonably well for some time periods, for other times the simple model boundary does not agree with observations. For instance, between 2015 July 29 and 2015 August 4 in Figure 8, the model predicted that *Rosetta* was supposed to be inside the diamagnetic cavity region, yet, as pointed out earlier, the observations show that the spacecraft in this time period was outside this region. The plasma environment of comet 67P/CG is highly complex and the diamagnetic regions cannot always be explained with a classic Halley-type diamagnetic cavity formalism. Some other mechanism might also be operating including perhaps electron temperature enhancements (Huang et al. 2016). Clearly, more work is needed on this topic.
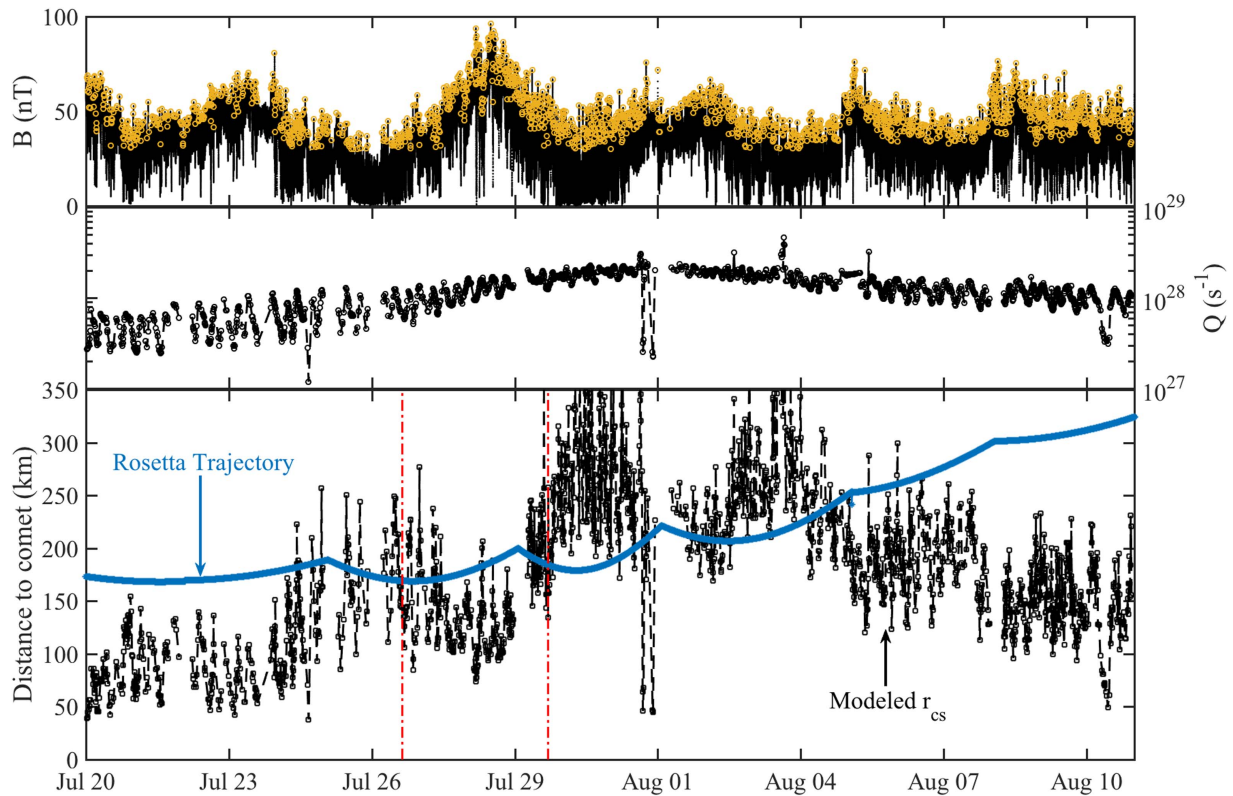
Figure 8. The top panel shows the magnitude of the magnetic field in black, and the yellow circles show the local maxima in the magnetic field. The middle panel shows the neutral outgassing rate measured by ROSINA/COPS. The bottom panel shows the *Rosetta* spacecraft distance to the comet (blue curve) and the estimated cavity boundary distance from 2015 July 20 to August 11 in black. The two red vertical lines on this panel mark the timestamps of two observed cavity crossing events considered earlier.

6. CONCLUSIONS

We analyzed *Rosetta* spacecraft observations of comet 67P/CG near perihelion. We showed moderately lower suprathermal electron fluxes inside the diamagnetic cavity than outside. The flux of electrons with energies between 40 eV to a couple of hundred eV shows a decrease inside the cavity, with more noticeable drops at energies around 60–100 eV and 150–250 eV. We do note again that other interpretations of the diamagnetic regions exist. For example, they could be highly localized regions with high plasma pressure, displacing the magnetic field (Huang et al. 2016). However, according to IES observations presented in the current paper, this pressure cannot come from the suprathermal electrons.

A possible reason for the lower electron fluxes in the cavity could be that solar wind suprathermal electrons are, somehow, obstructed from reaching inside the diamagnetic cavity. More specifically, the diamagnetic cavity is partially shielded from attenuated suprathermal solar wind electrons. Another possible explanation is that a lower solar wind dynamic pressure is required to have a diamagnetic cavity and that means lower suprathermal electron fluxes. Note that when the spacecraft is outside the cavity, higher fluxes are observed at higher magnetic field magnitudes (Figure 6), which is an indication that for a high magnetic field strength, there is a high solar wind dynamic pressure, which then correlates with high solar wind electron flux and density.

A comparison of the modeled spectra with the IES measurements in Figure 7 suggests that inside the cavity, coma photoelectrons (model case 1) are not sufficient to explain the

IES data and either a trapping mechanism and/or solar wind electrons are needed. In the energy range between 40 and 90 eV, the IES electron flux is lower than what model case 2 predicts, suggesting that there are obstacles for external (i.e., solar wind) electrons with those energies to reach inside the cavity boundary, in agreement with our earlier speculation.

Also, multiple diamagnetic cavity crossing events seen in Figures 2 and 4 and in Nemeth et al. (2016) and Goetz et al. (2016) can be attributed to the very dynamic solar wind conditions and the fact that during perihelion passage, the spacecraft distance to the comet was about and beyond 150 km and not inside the predicted diamagnetic cavity boundary (Koenders et al. 2015). Goetz et al. (2016) suggested that the most likely explanation for this moving/transient boundary is the existence of Kelvin–Helmholtz instabilities propagating tail-ward along the cavity surface. The transient nature of these events, however, makes it difficult to compare the observations at comet 67P/CG with other comets such as 1P/Halley.

REFERENCES

Balsiger, H., Altwegg, K., Boschler, P., et al. 2007, SSRv, 128, 745
Behar, E., Nilsson, H., Stenberg, G., et al. 2016, GeoRL, 43, 1411
Broiles, T. W., Burch, J. L., Clark, G. B., et al. 2015, A&A, 583, 21
Broiles, T. W., Livadiotis, G., Burch, J. L., et al. 2016, JGR, 121, 7407
Burch, J. L., Goldstein, R., Cravens, T. E., et al. 2007, SSRv, 128, 697
Burch, J. L., Gombosi, T. I., Clark, G., Mokashi, P., & Goldstein, R. 2015, GeoRL, 42, 6575
Carr, C., Cupido, E., Lee, C. G. Y., et al. 2007, SSRv, 128, 629
Coates, A. J. 2009, in Proc. 18th Annual Int. Astrophysics Conf. 1183, Bow Shocks at Comets. in Shock Waves in Space and Astrophysical Environments, ed. X. Ao, R. H. Burrows, & G. P. Zank (New York: AIP), 121
Coates, A. J., Johnstone, A. D., Kessel, R. L., et al. 1991, AdSpR, 11, 227
Coates, A. J., Mazelle, C., & Neubauer, F. M. 1997, JGR, 102, 7105
Cravens, T. E. 1986, in Proc. 20th ESLAB Symp. the Exploration of Halley's Comet, The Physics of the Cometary Contact Surface, ed. B. Battrick, E. J. Rolfe, & R. Reinhard (Eur. Space Agency Spec. Publ.), 244 SP-250
Cravens, T. E. 1989, AdSpR, 9, 293
Cravens, T. E. 1991a, in Comets in the Post-Halley Era, 2, ed. R. L. Newburn, Jr. et al. (Norwell, MA: Kluwer), 1211
Cravens, T. E. 1991b, in Cometary Plasma Processes, Vol. 61, ed. A. D. Johnstone (Washington D.C: AGU), 27
Cravens, T. E., & Gombosi, T. I. 2004, AdSpR, 33, 1968
Cravens, T. E., Kozyra, J. U., Nagy, A. F., et al. 1987, JGR, 92, 7341
Cravens, T. E., Lindgren, C. J., & Puhl, P. 1995, AdSpR, 16, 19
Damas, M. C., & Mendis, D. A. 1992, ApJ, 396, 704
Edberg, N. J. T., Alho, M., André, M., et al. 2016a, MNRAS, 462, S45
Eviatar, A., & Goldstein, B. E. 1988, JGR, 95, 1759
Flammer, K. 1993, in COSPAR Coll. 4, The Cometary Diamagnetic Cavity Boundary and Inner Shock, in Plasma Environments of Non-Magnetic Planets, ed. T. I. Gombosi (Oxford: Pergamon), 99
Flammer, K. R., Omidi, N., & Quest, K. B. 1991, GeoRL, 18, 369
Gan, L., & Cravens, T. E. 1990, JGR, 95, 6285
Glassmeier, K. H., Boehnhardt, H., Koschny, D., Kührt, E., & Richter, I. 2007a, SSRv, 128, 1
Glassmeier, K. H., Richter, I., Diedrich, A., et al. 2007b, SSRv, 128, 649
Goetz, C., Koenders, C., Richter, I., et al. 2016, A&A, 588, A24
Goldstein, B. E., Altwegg, K., Balsiger, H., Fuselier, S. A., & Ip, W.-H. 1989, JGR, 94, 17251
Gombosi, T. I. 2015, Magnetotails in the Solar System (Hoboken, NJ: Wiley)
Hansen, K. C., Altwegg, K., Berthelier, J.-J., et al. 2016, MNRAS
Hansen, K. C., Bagdonat, T., Motschmann, U., et al. 2007, SSRv, 128, 133
Huang, Z., Toth, G., Gombosi, T. I., et al. 2016, MNRAS, accepted
Ip, W.-H., & Axford, W. I. 1987, Natur, 325, 418
Koenders, C., Glassmeier, K.-H., Richter, I., Motschmann, U., & Rubin, M. 2013, P&SS, 87, 85
Koenders, C., Glassmeier, K. H., Richter, I., Ranocha, H., & Motschmann, U. 2015, P&SS, 105, 101
Korosmezey, A., Cravens, T. E., Gombosi, T. I., et al. 1987, JGR, 92, 7331
Madanian, H., Cravens, T. E., Rahmati, A., et al. 2016a, JGRA, 121, 5815
Madanian, H., Cravens, T. E., Richard, M. S., et al. 2016b, JGRA, 121, 8013
Mandt, K. E., Eriksson, A., Edberg, N. J. T., et al. 2016, MNRAS, 462, S9
Mendis, D. A., Houpis, H. L. F., & Marconi, M. L. 1985, FCPh, 10, 1
Nagy, A. F., & Banks, P. M. 1970, JGR, 75, 6260
Nemeth, Z., Burch, J., Goetz, C., et al. 2016, MNRAS submitted
Neubauer, F. M. 1988, JGR, 93, 7272
Neubauer, F. M., Glassmeier, K. H., Pohl, M., et al. 1986, Natur, 321, 352
Nilsson, H., Stenberg Wieser, G., Behar, E., et al. 2015a, Sci, 347, 571
Omidi, N., & Winske, D. 1987, JGR, 92, 13409
Puhl-Quinn, P., & Cravens, T. E. 1995, JGR, 100, 21631
Richter, I., Koenders, C., Auster, H.-U., et al. 2015, AnGeo, 33, 1031
Richter, I., Koenders, C., Glassmeier, K., Tsurutani, B., & Goldstein, R. 2011, P&SS, 59, 691
Rubin, M., Hansen, K. C., Combi, M. R., et al. 2012, JGR, 117, 227
Rubin, M., Koenders, C., Altwegg, K., et al. 2014, Icar, 242, 38
Vigren, E., & Galand, M. 2013, ApJ, 772, 33
Volwerk, M., Richter, I., Tsurutani, M., et al. 2016, AnGeo, 34, 1